Applied Catalysis B: Environmental 201 (2017) 70–76

Contents lists available at ScienceDirect

Applied Catalysis B: Environmental

journal homepage: www.elsevier.com/locate/apcatb

Biomimetic photoelectrocatalytic conversion of greenhouse gas carbon dioxide: Two-electron reduction for efficient formate production

Qi Shen, Xiaofeng Huang, Jibo Liu, Chenyan Guo, Guohua Zhao *

School of Chemical Science and Engineering, Shanghai Key Lab of Chemical Assessment and Sustainability, Tongji University, 1239 Siping Road, Shanghai 200092, China

ARTICLE INFO

Article history:
Received 23 June 2016
Received in revised form 29 July 2016
Accepted 3 August 2016
Available online 3 August 2016

Keywords:
Biomimetic photoelectrocatalysis
Cobalt-containing zeolite imidazolate framework
CO_2 Activation
CO_2 Reduction
Heterojunction

ABSTRACT

Resource utilization of carbon dioxide (CO_2) as alternative carbon feedstock is a promising solution to problems of both the energy supply and global warming. Herein, a biomimetic photoelectrocatalytic interface was covalently constructed utilizing cobalt-containing zeolite imidazolate framework (ZIF9) as CO_2 fixation and activation substrate, and Co_3O_4 nanowires (NWs) as the photoelectrocatalyst. Adsorption experiments demonstrated that CO_2 could be concentrated on ZIF9 modified Co_3O_4 NWs. The CO_2 surface concentration exhibited a 3.44 fold increment on this hybrid interface than that on Co_3O_4 NWs. Theoretical calculation elucidated ZIF9 has the capacity for activating CO_2 molecule via binding Co atom to the O atom of CO_2, resulting in the onset potential of CO_2 reduction 284 mV positively shift on ZIF9-Co_3O_4 NWs than that on Co_3O_4 NWs. At a low overpotential of 290 mV, CO_2 has been photoelectrocatalytically conversion to formate with high conversion rate of 72.3 $\mu mol\,L^{-1}\,cm^{-2}\,h^{-1}$ and high selectivity of nearly 100% in liquid products. And the heterogeneous electron transfer constant was 2.096×10^{-3} cm s^{-1}. This CO_2 conversion process was confirmed to be an instantaneous proton-coupled 2-electron transfer process. This work opens the opportunity for constructing biomimetic photoelectrocatalytic interface with CO_2 adsorption, activation and conversion to efficient CO_2 resource utilization.

© 2016 Elsevier B.V. All rights reserved.

1. Introduction

Since the industrial revolution, fossil fuel combustion has rapidly increased the atmospheric greenhouse gases levels, leading to the most drastic environmental concern associated with global warming, climate change and seawater acidification [1,2]. In addition, depletion of fossil fuel resources along with unsustainable carbon emission threatens to create an energy crisis. Carbon dioxide (CO_2) as one of the most main greenhouse gases and a kind of potential carbon resource, the conversion of CO_2 into high value-added industrial chemicals and hydrocarbon fuels has been referred to as "reverse combustion" and persistently drawing attention [3].

In nature, the photosynthesis of green leaves can utilize solar energy to convert water and carbon dioxide into carbohydrates and oxygen [4]. This conversion process is an integrated system in which light harvesting, photoinduced charge separation, CO_2 fixation and catalysis are combined. Inspired by natural leaves, many efforts have been devoted to developing artificial photocatalysts or photoelectrocatalysts for achieving direct conversion of sunlight and CO_2 into chemical fuels [5–7]. Up to date, a large number of metal oxide semiconductors, such as TiO_2-based materials [8,9], $ZnCo_2O_4$ [10], $SrTiO_3$ [11] and so forth, have been reported that they have the ability to reduce CO_2 [12]. However, the catalytic efficiency is still not satisfactory due to the CO_2 limited adsorption and activation ability of semiconductor. The relative stability ($\Delta G_f^\theta = -394.4\,kJ\,mol^{-1}$) and high single electron reduction energy (-1.9 eV vs normal hydrogen electrode, NHE) of CO_2 lead to a high reorganization energy of the CO_2 reduction reaction [3]. Activation of CO_2, as the first step in CO_2 reduction, is manifested mostly in the bending of the CO_2 molecule, which could considerably lower the activate energy of CO_2 reduction [1]. As is known, a net transfer of electron density from metal to CO_2 will happen when CO_2 is coordinated to transition metals, which results in an activation state of CO_2. For instance, five possible structures for adsorbed CO_2 on Cu metal was explored [13]. For each kind of structure, CO_2 molecular is activated by structure bent. And molecular catalyst, such as Ru and Re complexes, also tends to activate CO_2 by coordinating CO_2 with the central metal atoms [14].

* Corresponding author.
E-mail address: g.zhao@tongji.edu.cn (G. Zhao).

http://dx.doi.org/10.1016/j.apcatb.2016.08.008
0926-3373/© 2016 Elsevier B.V. All rights reserved.

Encouragingly, metal–organic frameworks (MOFs) are a class of materials with central metal atoms and have impacts on CO_2 transition from linear state to bent one. A Cu porphyrin based MOF has been proved to deform CO_2 molecule, and the CO_2 photoreduction barrier was lowered [15]. Notably MOFs are a class of three-dimensional (3D) porous hybrid materials, possessing high specific surface area, acceptable CO_2 selective adsorption and separation ability [16–18]. Heterogeneous MOFs catalysts have been applied for CO_2 photocatalysis and electrocatalysis, like CR-MOF [19], NH_2-MIL-125(Ti) [20], NH_2-Uio-66(Zr) [21], cobalt-containing Zeolite Imidazolate Framework (ZIF9) [22,23]. Nevertheless, the catalytic performance of MOFs is far from satisfaction compared to metal oxides due to the low efficiency in electron excitation and charge separation.

Herein, we aim to design a biomimetic photoelectrocatalytic (PEC) platform by introducing MOFs materials to the semiconductor-based PEC system. On one hand, appropriate MOFs will facilitate selective adsorption and fixation of CO_2, enhance surface CO_2 concentrations and lower the activation energy of the reaction while achieving efficient CO_2 reduction reaction on the dynamics. On the other hand, PEC process combines the merits of both electrocatalysis and photocatalysis, proposing a more promising approach to the separate photo-induced charge carriers, reduce the CO_2 activation barrier and promote CO_2 conversion. Recently, efforts have been made to integrate MOFs with inorganic semiconductor to improve the CO_2 fixation and activation of inorganic materials. For instance, Zn_2GeO_4/ZIF-8 hybrid nanorods [24] and $Cu_3(BTC)_2$@TiO_2 core-shell structures [25] have been fabricated and applied to CO_2 photocatalytic reduction with dramatically improved performance in terms of both activity and selectivity. To further enhance PEC activity of CO_2 reduction, we wondered if tight integration between semiconductor and MOFs could effectively promote the PEC performance of materials. It is notable that ZIF9 is a microporous crystalline material composed of Co (II) ions linked to benzimidazolate, with a high specific surface area of 1607 $m^2\,g^{-1}$ and considerable adsorption capacity to gaseous CO_2 of 2.7 $mmol\,g^{-1}$ [26]. It has been used as a co-catalyst for photocatalytic reduction of CO_2 to CO [22,26]. It is interesting that similar to ZIF9, Co_3O_4 as a cobalt-based spinel is not only cheap, abundant and excellent environmental stability, but also has been proved to be effective in selective catalytic reduction of CO_2 to formic acid [27–30]. Therefore, an outstanding biomimetic PEC platform was constructed by a self-template for CO_2 resource utilization, subtly utilizing Co^{2+} in-situ dissolved from Co_3O_4 NWs coordinate with ligand to covalent growth of ZIF9 layer on Co_3O_4 NWs, see Fig. 1A. In which, ZIF9 is in the upper layer as a "stoma" for CO_2 fixation and activation, and Co_3O_4 nanowires (NWs) is in the lower layer as the photoelectrocatalyst. Driven by external electric field and the *p-p* heterojunction between ZIF9 and Co_3O_4 NWs, photo-induced electrons rapidly transfer to the electrode surface to react with CO_2. And formate was produced in an 8 h photoelectrochemical process with comparatively high conversion rate and its selectivity was up to 99% in liquid products.

2. Experimental section

2.1. Chemicals and materials

Fluorine-doped tin oxide transparent conductive film glass (FTO) was purchased from Nippon Sheet Glass Co. Ltd., and $Co(NO_3)_2{\cdot}6H_2O$, urea, ammonium fluoride (NH_4F), Na_2SO_4, benzimidazole and DMF were all analytical reagent and purchased from Sinopharm Chemical Reagent Co., Ltd., SCRC, China.

2.2. Construction of biomimetic photoelectrocatalytic interface

All the biomimetic PEC interfaces were prepared on FTO. Before experiment, FTO was cleaned via ultrasonication in deionized water, mixed organic solvents (isopropanol: acetone: H_2O = 1:1:1) and ethanol successively.

In a typical solvothermal synthesis of Co_3O_4 NWs electrode, 2.93 g of $Co(NO_3)_2{\cdot}6H_2O$, 0.74 g of NH_4F, and 3.00 g of urea were orderly dissolved in a 70 mL deionized water under magnetic stirring for half an hour. After a homogeneous solution was formed, the solution was transformed to a Teflon-lined stainless steel autoclave in which a FTO glass with $1.5 \times 4.0\,cm^2$ in size was added. The autoclave was heated at 120 °C for 9 h, and then cooled down to room temperature naturally. The as-prepared electrode was rinsed with deionized water three times and then dried in N_2 atmosphere, followed by a calcination process in a N_2 atmosphere at 450 °C for 2 h under a ramping rate of 5 °C.

ZIF9 was prepared as following procedure [22]: firstly, $Co(NO_3)_2{\cdot}6H_2O$ (0.210 g, 7.21×10^{-4} mol) and benzimidazole (0.060 g, 5.08×10^{-4} mol) were orderly dissolved in 18 mL DMF under magnetic stirring. After stirring for 1 h, the resulting solution was transformed to a 25 mL Teflon-lined stainless steel autoclave. The autoclave was then heated to 130 °C from the room temperature with a ramp of 5 °C·min^{-1} in a programmed oven. After a 48 h reaction, the autoclave cooled down to room temperature naturally. Finally, the obtained purple crystal were washed thrice with DMF and dichloromethane respectively, and dried in a vacuum drying box.

The growth of ZIF9 on the Co_3O_4 NWs electrode proceeded via a simple chemical bath route. Typically, 0.18 g benzimidazole was dissolved with a 48 mL mixed solvent of DMF/H_2O at different ratios (4:1, 3:1, 2:1 and 1:1), and then was transformed to a Teflon-lined stainless steel autoclave. The autoclave was maintained at 70 °C for 24 h after a piece of Co_3O_4 NWs electrode was immersed. The atropurpureus ZIF9-Co_3O_4 NWs electrode was obtained and washed thrice with DMF and dichloromethane respectively in order to remove the residual benzimidazole. For comparison ZIF9 electrode was prepared on FTO glass. ZIF9 (3 mg) and Nafion solution (40 μL) were mixed with 1 mL ethanol. After a sonication for 30 min, obtained slurry was spread onto the FTO glass, and the electrode was then dried under vacuum.

2.3. Characterization

The morphology of the as-prepared electrodes were characterized by field-emission scanning electron microscopy (FE-SEM, Hitachi S-4800, Japan) and transmission electron microscopy (TEM, JEM-2100, JEOL, Japan). X-ray diffractometer (XRD, D/max2550VB3+/PC, Rigaku International Corporation, Japan) was carried out to determine the crystalline structures of Co_3O_4 NWs, ZIF9 and ZIF9-Co_3O_4. Surface elemental analysis of Co_3O_4 and ZIF9-Co_3O_4 were performed on an X-ray photoelectron spectroscopy (XPS, AXIS Ultra HSA, Kratos Analytical Ltd., UK). The binding energies obtained in the XPS were all corrected by referencing the carbon 1 s peak to 284.7 eV. The optical absorption properties were investigated by AvalightDHS UV–vis absorbance measurements (UV-DRS, Avantes, Netherlands).

In situ Fourier transform infrared (FT-IR) spectra were recorded on a FT-IR spectrometer (Nicolet 8700, Thermo Fisher Scientific Inc. USA). Before spectra detection, the mercury-cadmium-telluride detector was cooled down to 77 K by liquid nitrogen. All of the samples were treated at 70 °C in a vacuum drying chamber overnight to remove the adsorbed gas molecules. Then the spectra were collected using a sample cell equipped with CaF_2 window at normal temperature and atmospheric pressure (25 °C and 1 atm). CO_2 was inlet into the sample cell slowly and continuously and one hundred

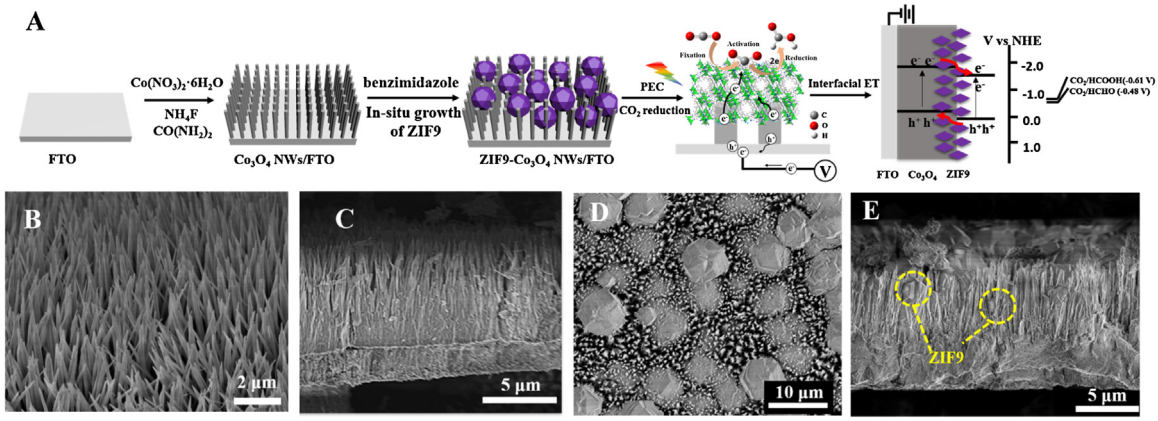

Fig. 1. (A) Schematic representation of the fabrication of ZIF9-Co_3O_4 NWs and proposed mechanism of PEC reduction of CO_2 on ZIF9-Co_3O_4 NWs; (B) SEM image of top view of the Co_3O_4 NWs. (C) SEM image of side view of Co_3O_4 NWs. (D) SEM image of top view of the ZIF9- Co_3O_4 NWs. (E) SEM image of side view of ZIF9-Co_3O_4 NWs.

IR spectra were collected with a spectrum resolution of 8 cm^{-1}. The spectra under N_2 atmosphere were collected for comparison.

Theoretical calculations were carried out using density functional theory (DFT) as implemented in Gaussian 09. Tao-Perdew-Staroverov-Scuseria (TPSS) functional was used with LanL2DZ basis set for Co atom and all-electron 6–31G (d, p) basis set for H, C, N, O atoms. The geometric configurations of all species were optimized at their gas phase states.

All PEC measurements were performed on a CHI 660C electrochemical workstation (CH Instruments, Inc.) using a conventional three electrode system with the as-prepared electrodes as working electrodes, saturated calomel electrode (SCE) as reference electrode, and a platinum foil as counter electrode in 0.1 M Na_2SO_4 aqueous solution. Linear sweep voltammetry (LSV) was performed from the potential range of 0 to −1.2 V at a scan rate of 0.05 V s^{-1}. The amperometric *i–t* curve was recorded at a constant potential of−0.9 V with an interval of 100 s for light on/off (light source: LA-410UV with UV cutoff, Hayashi, Japan).

2.4. PEC CO_2 reduction and product analysis

The PEC reduction of CO_2 was performed in an H-type two chamber reactor, which was separated with the Nafion-117 proton exchange membrane (DuPont). Before reduction, high purity CO_2 (99.99%) gas was bubbled at a flow rate of 20 mL min^{-1} into the 0.1 M Na_2SO_4 solution until the concentration of CO_2 reached saturation and the dissolved oxygen was removed completely. The concentration of free CO_2 measured by acid-base titration was 0.0331 M and the pH of the solution was 4.11. The potential during the PEC reduction was kept constant at −0.9 V under 100 mW cm^{-2} irradiation (light source: PLS-SXE300 xenon lamp, Beijing Perfect-Light Co., Ltd., China, with AM 1.5).

Nash's colorimetric method was applied to quantify the yield of formic acid and formaldehyde in liquid products. For the detection of formaldehyde, 2.0 mL liquid product was directly mixed with 2.0 mL Nash's reagent (25 g ammonium acetate, 2.1 mL glacial acetic acid, and 0.2 mL acetylacetone dissolved in 100 mL ultrapure water). The mixture was shaken for 1 h, and analyzed by UV−vis spectroscopy (UV8453, Agilent) at the absorption wavelength of 414 nm. Formic acid was reduced to formaldehyde firstly and then quantified by Nash's colorimetric method. Briefly, 50 mg magnesium ribbon was added into 0.5 mL of liquid sample. And then 0.5 mL of concentrated hydrochloric acid (37%) was added dropwise into the above mixture with vigorous stirring at 0 °C. Afterward, 3 mL of 1 M NaOH was added into the above solution to remove the residual Mg^{2+}. The obtained suspension was then centrifuged at 10,000 rpm for 5 min, and supernatant was mixed with 2 mL Nash reagent for UV–vis spectroscopy analysis. The amount of HCOOH was obtained by subtracting the amount of HCHO in the product. The other products in liquid and gas products were determined by gas chromatograph (GC) equipped with thermal couple detector (Techcomp, China).

3. Results and discussion

Sustained PEC CO_2 reduction by simulated solar light was conducted to verify the efficiency of conversion CO_2 into value-added hydrocarbon on biomimetic PEC system. Formate was detected as the dominant product in liquid, with a small amount of formaldehyde. As shown in Fig. 2A, with the ZIF9-Co_3O_4 NWs electrode, the amount of formate reached 578.7 μmol L^{-1} cm^{-2} in 8 h, nearly 1.6 and 2.9-folds higher than that at Co_3O_4 NWs electrode (364.3 μmol L^{-1} cm^{-2}) and ZIF9 electrode (199.6 μmol L^{-1} cm^{-2}). If taking the reduction time span further into account, the conversion rate of CO_2 to formate reached nearly 72.3 μmol L^{-1} cm^{-2} h^{-1}. Trace amounts of formaldehyde were detected at all of those electrodes: 2.2 μmol L^{-1} cm^{-2} (ZIF9), 3.9 μmol L^{-1} cm^{-2} (Co_3O_4 NWs) and 4.9 μmol L^{-1} cm^{-2} (ZIF9-Co_3O_4 NWs). It indicated a high selectivity of ~99% to formate in liquid products from CO_2 was achieved.

A complete comparison of the CO_2 reduction performance with literature reports are summarized in Table 1. As we can see, the yield of formate on our biomimetic PEC interface is higher than most of reported values, where the main product was formate/formic acid in either photocatalytic, electrocatalytic or PEC processes. More importantly, the yield of formate is also higher than that on some heterogeneous semiconductor-molecular catalyst system [31–37], which is a promising artificial system for the CO_2 reduction. And the estimated faradaic efficiency for yield formate is about 70.5% on our biomimetic PEC system, which is comparable to that on some semiconductor based photocatalytic system like Mg-doped $CuFeO_2$ [38] and Pyridine-CdTe/FTO [35] as well as on heterogeneous semiconductor-molecular catalyst PEC systems like InP/[MCE2-A + MCE4] [36] and [RuCE + RuCA]/CZTSSe [34]. Furthermore, up to an 8 h sustained PEC CO_2 reduction, the photocurrent density showed no noticeable sign of decrease, indicating the ZIF9-Co_3O_4 NWs electrode has an outstanding PEC stability (Fig. S1).

As is known to all, CO_2 adsorption is of the greatest concern during the whole CO_2 reduction process and the adsorption performance is tightly intertwined with the architecture of catalytic system. In this work, Co_3O_4 NWs was firstly prepared on a piece of FTO by hydrothermal process. As seen in Fig. 1B and C, a well-aligned, upright 1D NWs layer grew successfully on the FTO. The thickness of Co_3O_4 NWs layer was ca. 6.0 μm and the diameter was ca. 160–170 nm (Fig. S2). Additionally, the single nanowire

Table 1
Formate yields in comparison to some systems reported for the reduction of CO_2.

Catalyst	Condition	Products	Yield of $HCOO^-$	Faradic efficiency	Ref.
ZIF9-Co_3O_4 NWs	−0.9 V, Xe lamp (100 mW AM 1.5), 8 h.	$HCOO^-$, HCHO (few)	578.7 μmol L^{-1} cm^{-2}	70.5%	
{12$\bar{1}$}Co_3O_4	−0.9 V, Xe lamp (9 mW cm^{-2}), 8 h.	HCOO-	384.8 ± 7.4 μmol	–	[27]
RuP/C_3N_4	400 W high-pressure Hg lamp, 20 h.	$HCOO^-$, CO, H_2	67.7 μmol	–	[31]
Ru(dcbpy)$(CO)_2Cl_2$/p-InP-Zn	−0.6 V vs Ag/AgCl, Xenon light,3 h.	$HCOO^-$	170 μmol.L^{-1}	62.3%	[32]
Ag/TaON−RuBLRu'	500-W Hg lamp (l < 400 nm), 15 h.	HCOO-, CO, H_2	969 nmol	–	[33]
[RuCE + RuCA]/CZTSSe	−0.4 V vs Ag/AgCl, Xenon light, 3 h.	$HCOO^-$, CO, H_2	490 μmol.L^{-1}	80%	[34]
Mg doped $CuFeO_2$	−0.4 V vs SCE, blue LED (470 nm, 2.1 mW cm^{-2}).	$HCOO^-$, H_2	–	10%	[38]
Pyridine-CdTe/FTO	−0.6 V, Xe-arc lamp (450W), 6 h.	HCOOH	167 μmol	60.7%	[35]
InP/[MCE2-A + MCE4]	−0.4 V vs Ag/AgCl, Xenon light (l > 400 nm), 24 h.	HCOO-, CO, H_2	40 μmol cm^{-2}	80%	[36]

"–" in the column of "Yield of $HCOO^-$" and "Faradic efficiency" means it is not mentioned in Reference.

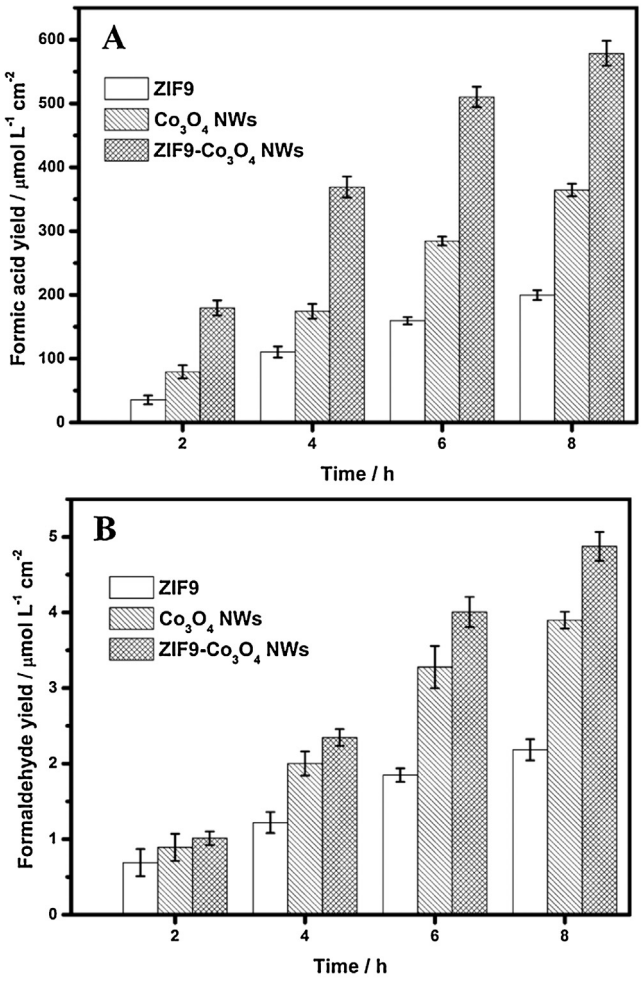

Fig. 2. Formate yields (A) and Formaldehyde yields (B) under PEC condition with the reduction time on ZIF9, Co_3O_4 NWs, and ZIF9-Co_3O_4 NWs electrode.

was composed of numerous interconnected Co_3O_4 nanoparticles, which increases the surface area of this material. Afterwards, ZIF9 layer as CO_2 acceptor for CO_2 fixation and activation was in situ grown on Co_3O_4 NWs by a chemical bath. The growth process by a self-template strategy depends on the hydrothermal solvent composition [39]. Different volume ratios of solution composition (DMF/H_2O) were considered in our study, shown in Table S1. Taking into account the synergies of optical absorption, CO_2 adsorption and activation, the DMF/H_2O ratio of 2:1 was selected as the preparation condition. As shown in Fig. 1D, E. ZIF9 grew evenly on Co_3O_4 NWs layer as well as embedded in Co_3O_4 NWs, and the average particle size of ZIF9 is ca. 10 μm.

In the course of subsequent studies, the adsorption enhancement of ZIF9 to CO_2 was investigated. The surface concentration of CO_2 (Γ_{ads}), normalized amount of adsorbed CO_2 with the electrochemical active surface area (S_{EASA}), was adopted to evaluate the efficiency of CO_2 fixation. The S_{EASA} of ZIF9-Co_3O_4 NWs is 612.5 calculated from Fig. S4, 2.2-fold increment than that of Co_3O_4 NWs (283.1). And the electroactive CO_2 adsorption amounts calculated from Fig. S5 is 4.82×10^{12} cm^{-2} on Co_3O_4 NWs, corresponding to a Γ_{ads} of 1.70×10^{10} cm^{-2}. And the CO_2 adsorption amounts on ZIF9-Co_3O_4 NWs is 3.59×10^{13} cm^{-2}, corresponding to a Γ_{ads} of 5.86×10^{10} cm^{-2}, 3.44 fold increment than that of Co_3O_4 NWs. It is indicated that combination of ZIF9 can significantly promote CO_2 adsorption performance of Co_3O_4 NWs, which will help improve the CO_2 reduction efficiency.

DFT calculation method was then applied to theoretical analysis CO_2 activation performance on the ZIF9. As shown in Fig. 3A, ZIF9 is composed of Co (II) ions coordinated by nitrogen atoms in benzimidazolate and adopts a microporous crystalline structure with 4.31 Å in aperture size [16], larger than the size of CO_2 molecular (2.32 Å). As depicted by DFT calculations results, once the linear CO_2 molecule is adsorbed into ZIF9 micro-pore structure, it will be turn to a bent form. Due to the interaction between the O atom of CO_2 and Co atom of ZIF9, bond angle of O–C–O is transferred to 134.2° from 180.0°, and the distance of C–O in bent CO_2 are stretched to 1.236 Å and 1.276 Å longer than that (1.160 Å) of the linear CO_2 molecule (Fig. 3B). The bent structure can lower energy level difference between highest occupied molecular orbitals (HOMO) and lowest unoccupied molecular orbitals (LUMO) of CO_2 molecular, and the activation energy is reduced by 43.83%. Most importantly, the Gibbs energy of the bent CO_2-ZIF9 molecule is only raised by 3.398 kcal mol^{-1} than that of linear CO_2-ZIF9 (Fig. 3C), indicating the activation barrier for this key step is very low and CO_2 activation is achieved on ZIF9.

In order to verify the bent CO_2-ZIF9 form from was further confirmed from DFT calculation, in situ FT-IR spectra was conducted to capture this intermediate state. As shown in Fig. 3D, a plainly visible peak at 1770 cm^{-1} could be found under a CO_2 atmosphere compared with that under a N_2 atmosphere, which belongs to the asymmetric stretching vibrations ν_{as}(OCO) of the "end-on" coordination mode [15]. This result is consistent with the DFT calculation, indicating the linear CO_2 molecular could be chemically adsorbed on the ZIF9 in the form of Co-O bond and bend. It is can be explained by electronic cloud distribution on the singly occupied molecular orbital (SOMO). As shown in Fig. 3B, the electronic cloud distribute in both CO_2 and ZIF9 in the bent type, while it mainly distribute in the ZIF9 (Table S2) in the linear type. It is indicated that after ZIF9 adsorb CO_2, the electron is easily transferred from ZIF9 to CO_2, leading to the formation of bent CO_2 molecular. As a result, the energy difference between HOMO and LUMO of CO_2 molecular is lowered and CO_2 molecular is activated.

Furthermore, light absorption property is another key concern to the PEC process. UV diffraction reflection spectroscopy (UV-DRS)

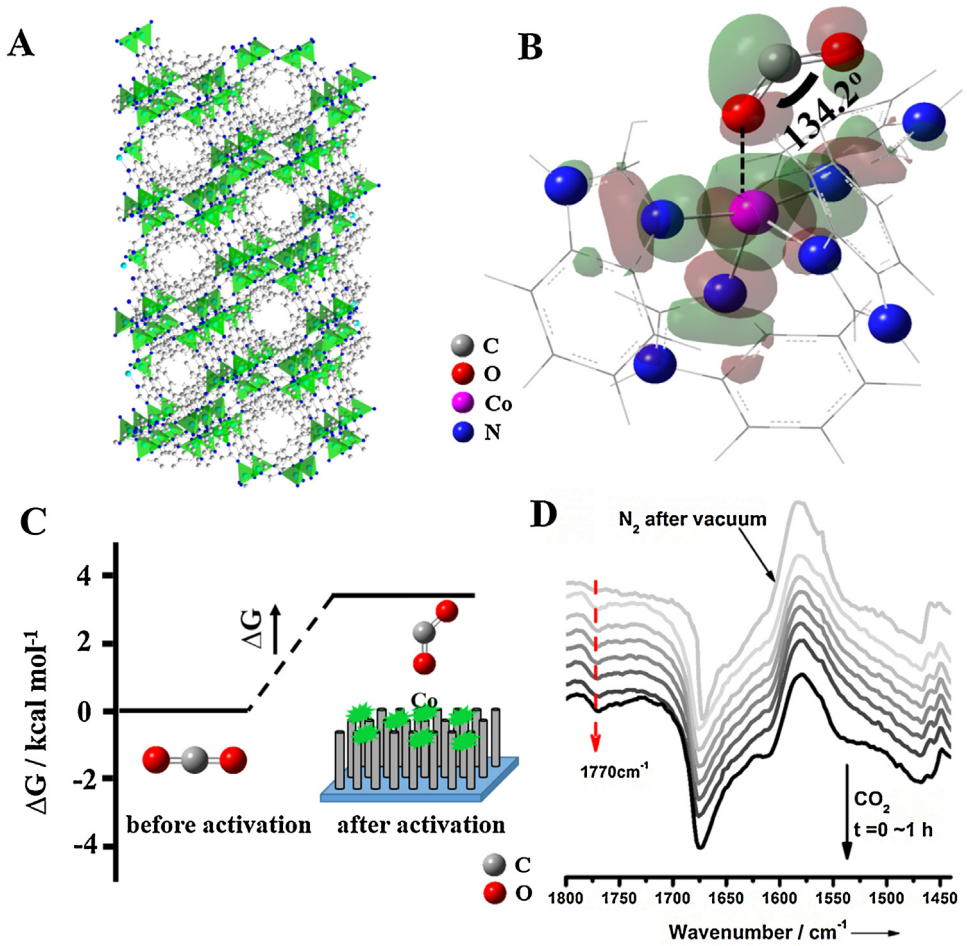

Fig. 3. (A) View of the 3D network of ZIF9 through the c-axis. (B) SOMO orbit of the bent CO_2-ZIF9 molecule. (C) DFT calculated Gibbs energetic difference between linear and bent adsorbed CO_2-ZIF9. (D) Diffuse reflectance infrared Fourier transform spectroscopy (DRIFT) spectra of ZIF9 under N_2 and CO_2.

was applied to investigate the optical absorption property (Fig. 4A). Two broad absorption bands were observed at wavelengths of 300–550 and 600–800 nm for Co_3O_4 NWs, which could be assigned to the Co^{2+}–O^{2-} and the Co^{3+}–O^{2-} transition, respectively. And for the ZIF9, two broad absorption bands also could be observed at wavelengths of 300–400 and 400–700 nm. After ZIF9 growing on the Co_3O_4 NWs, the absorption in the ultraviolet and visible spectral range became stronger and broader than the individual Co_3O_4 NWs and ZIF9. The band gaps of Co_3O_4 NWs and ZIF9 calculated from Fig. S6 were 1.88 and 1.95 eV, respectively. Apparently, these bands gaps demonstrate that ZIF9-Co_3O_4 NWs has excellent light absorption capacity, and can be excited by sunlight to generate electron–hole pair. The flat-band potential of Co_3O_4 NWs was estimated to be −0.19 V vs SCE, and that of ZIF9 was estimated to be 0.1 V vs SCE (Fig. 4B). Based on the assumption that the valence band (VB) position is 0.1–0.2 V lower than the flat-band potential for a *p*-type semiconductor [38], the VB of Co_3O_4 NWs was estimated to be 0.05 to −0.15 V vs NHE. Thus, the conduction band (CB) edge of Co_3O_4 NWs was located at −1.93 to −2.03 V vs NHE. Similarly, the CB of ZIF9 was estimated to be at −1.81 to −1.71 V vs NHE, lower than that of Co_3O_4 NWs. It indicated that a *p-p* type heterojunction was formed between Co_3O_4 and ZIF9, and photoelectron could transfer from CB of Co_3O_4 to that of ZIF9. Energy level of CB with −1.81∼−1.71 eV is significantly higher than the reduction potential of CO_2 to HCOOH (-0.250 V vs NHE) and HCHO (-0.070 V vs NHE), and is conducive to the reduction of CO_2 to C1 products. Therefore, in this work, upright Co_3O_4 NWs can act as an "antenna" for solar light absorption and an electronic delivery channel for rapidly photo-generated electron migration to active sites. After the in-situ growth of ZIF9, Co_3O_4 NWs is tight-knit combined with the ZIF9 and not fully covered by ZIF9, see Fig. 1D. So the absorption of incident light could be ensured and photo-generated electron migrate rapidly to reaction activate sites through 1 D NWs.

Moreover, PEC CO_2 reduction performance of biomimetic PEC system was investigated. As shown in Fig. 5A and Fig. S7, the linear sweep voltammetry (LSV) trace of ZIF9-Co_3O_4 NWs photocathode showed the onset potential observed here of ZIF9-Co_3O_4 NWs was −0.338 V vs NHE, approximately 284 mV more positive than that at the Co_3O_4 NWs electrode. And the overpotential was only 299 mV at a current density of 1 mA cm^{-2}, which is lower than that of nanostructured tin catalyst (340 mV) [40] and Mg-doped $CuFeO_2$ photocathode (400 mV) [38]. Furthermore, a significant enhanced current density under a CO_2-saturated solution relative to that under a N_2-saturated solution. Similarly, the *i*–t curves (Fig. 5B) of both Co_3O_4 NWs and ZIF9-Co_3O_4 NWs electrodes show 3-fold enhanced photocurrent under CO_2-saturated solution than that under N_2-saturated solution. And under the CO_2-saturated solution, the photocurrent of ZIF9-Co_3O_4 NWs electrodes was 0.133 mA cm^{-2}, which is 2.4 orders of magnitude higher than that of Co_3O_4 NWs electrode (0.056 mA cm^{-2}).

In addition, heterogeneous electron transfer rate constant (k_s) for CO_2 reduction was calculated by LSV according to the following Equation [41]:

$$k_{s_{25^oC}} = 1.11 D_0^{1/2} (E_p - E_{p/2})^{-1/2} \nu^{1/2} \quad (1)$$

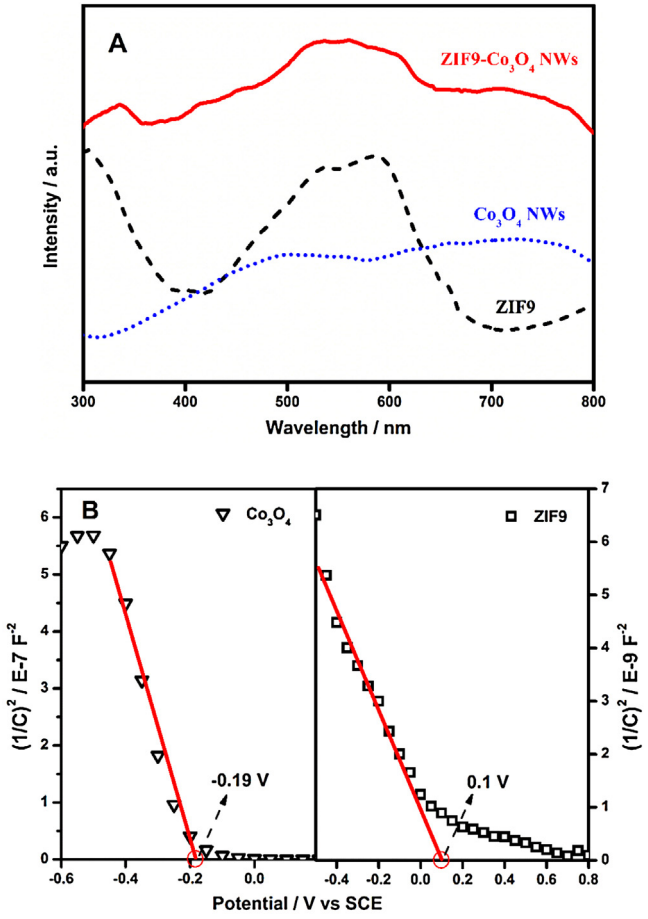

Fig. 4. (A) UV-DRS of ZIF9, Co_3O_4 NWs, and ZIF9- Co_3O_4 NWs. (B) Mott-Schottky plots of ZIF9 and Co_3O_4 NWs.

With ZIF9-Co_3O_4 NWs electrode, k_s is 2.096×10^{-3} cm s^{-1}, which is 21% bigger than that (1.731×10^{-3} cm s^{-1}) for Co_3O_4 NWs, indicating the combination ZIF9 with Co_3O_4 NWs is benefit for rapid separation of photo-generated carriers. It could be attribute to the covalent union between ZIF9 on Co_3O_4 NWs, which promote electron transfer between ZIF9 and Co_3O_4 NWs. X-ray photoelectron spectroscopy (XPS) analysis confirmed the combination of ZIF9 and Co_3O_4 NWs in ZIF9-Co_3O_4 NWs hybrid (Fig. S8). For Co 2p regions of ZIF9-Co_3O_4 NWs XPS spectrum, they can be fitted into six contributions. The presence of the peaks around 779.7 and 782.23 eV suggest that Co (II) exist in two coordination environments. The main peak at binding energies of 779.7 eV for the Co 2p3/2 lines is assigned to the Co of Co_3O_4 NWs, as seen in Fig. S5. The Co (II) 2p3/2 lines of ZIF9 lies at binding energies of 782.23 eV with a shakeup satellite at around 786.2 eV, and has a positive shift compared with that of Co_3O_4 NWs due to the coordination role of the N atom to Co atom. It is indicated that the combination of Co_3O_4 and ZIF9 are not simply by molecular bonding forces or physical adsorption, it is through a covalent bond between Co and N, which is benefit to the rapid electronic transfer within this system, as well as the improvement the stability of ZIF9-Co_3O_4 NWs material itself. XRD patterns, Raman and FTIR spectra of ZIF9-Co_3O_4 NWs were also conducted to confirm the junction of ZIF9 and Co_3O_4 NWs, as shown in Fig. S9, S10 and S11.

As investigated above, the roots for enhanced PEC activity toward CO_2 reduction on our biomimetic PEC system could be contributed to the following three aspects: (1) preferred binding to CO_2 on ZIF9 than water lead to an enhanced CO_2 surface concentration. (2) CO_2 can be activated after being adsorbed on ZIF9-Co_3O_4

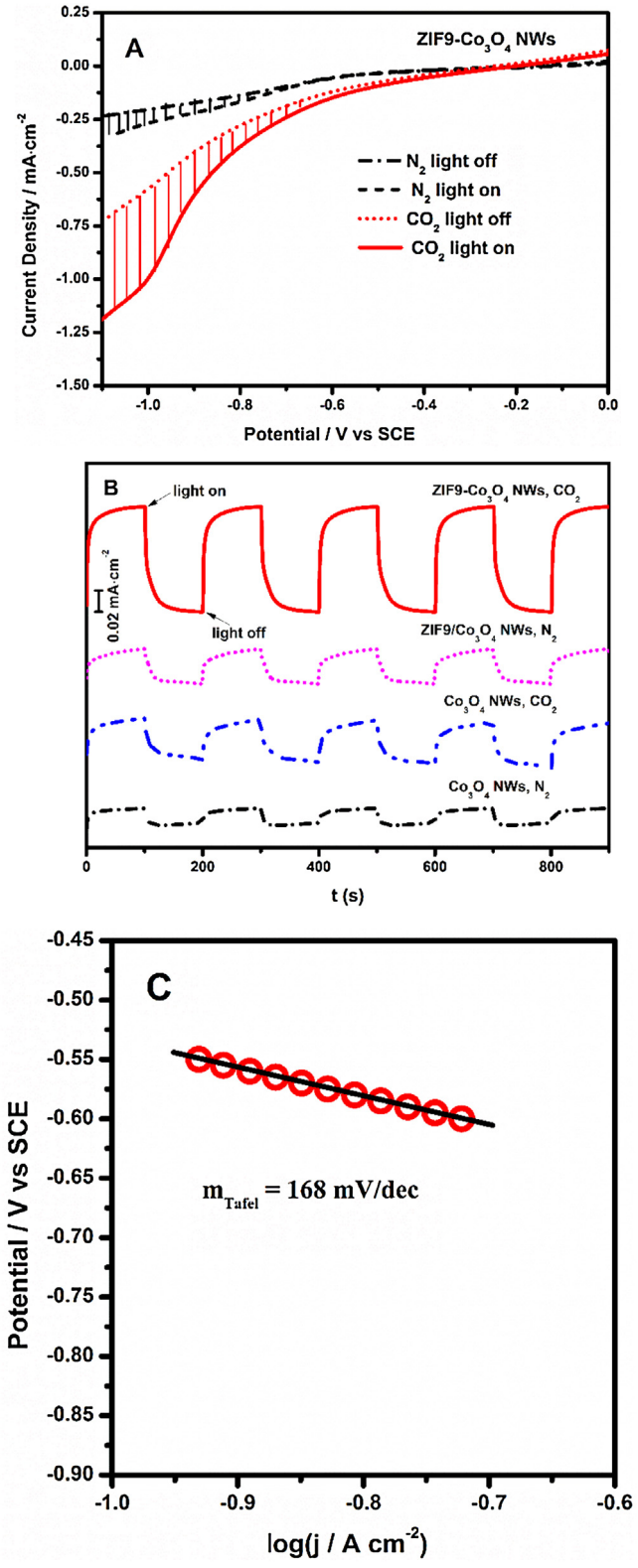

Fig. 5. (A) LSV of ZIF9-Co_3O_4 NWs electrode in N_2 or CO_2-saturated 0.1 M Na_2SO_4 solution under light on/off. (B) Amperometric i–t curves of Co_3O_4 NWs and ZIF9-Co_3O_4 NWs in N_2 and CO_2-saturated 0.1 M Na_2SO_4 at−0.9 V with light on/off. (C) Tafel plots of ZIF9-Co_3O_4 NWs electrode in CO_2-saturated 0.1 M Na_2SO_4 solution with light irradiation.

NWs, which lowers the CO_2 reduction overpotential and increases kinetics of CO_2 reduction than water/proton reduction on the active sites. (3) The covalent combination between ZIF9 and Co_3O_4 NWs is benefit for rapid separation of photo-generated carriers, promote the transfer of photoelectron, and improve the PEC ability to CO_2 reduction.

The possible mechanism of CO_2 conversion process was explored. Firstly, as mentioned above, the linear CO_2 molecular could be chemically adsorbed and activated on ZIF9 in the form of the "end-on" coordination mode. A PEC Tafel plots of ZIF9-Co_3O_4 NWs electrode display a slope of 168 mV/decade (Fig. 5C), indicating that the rate-determining step of CO_2 reduction was likely the first electron reduction to form a one electron reduction of a Co (II)-CO_2 adduct [42], which is also consistent with the DFT calculation and in situ FT-IR spectra results. Through a *p-p* heterojunction between ZIF9 and Co_3O_4 NWs, rapid electrons transfer from Co_3O_4 NWs to Co (II)-CO_2 adduct and a $HCOO^{-*}$ (* denotes activated state) is formed involving a proton electron coupling step. In the following step, a second electron rapidly transfers to $HCOO^{-*}$, resulting in desorption of $HCOO^-$ from the catalyst surface [30]. It is reported that the main product of CO_2 photoreduction in MeCN/H_2O using ZIF9 as photocatalysts is CO [22]. In our biomimetic PEC system, the assistance of electric field and Co_3O_4 catalyst [30] make catalytic sites nearby with more electron and proton, leading CO_2 reduction towards the $2e/2H^+$ reaction.

4. Conclusions

To sum up, in order to resource utilization of CO_2, a biomimetic PEC interface was constructed by utilizing ZIF9 covalently immobilized Co_3O_4 NWs. Such a biomimetic PEC interface effectively integrate CO_2 adsorption and activation capacity of the ZIF9 with excellent PEC CO_2 reduction performance of 1D Co_3O_4 NWs into one material, and has been applied in efficiently PEC $2e/2H^+$ reduction of CO_2 to formate by simulate sunlight. As light absorption antenna, Co_3O_4 NWs has well-aligned, upright 1D NWs structure, facilitating the separation of photogenerated electron-hole pair and rapid transfer of electrons to reaction active sites. And ZIF9 has the excellent capacities of CO_2 adsorption and activation. When Co_3O_4 NWs is covalently immobilized by ZIF9, an increased CO_2 adsorption could be achieved. Moreover, a *p-p* heterojunction between ZIF9 and Co_3O_4 NWs greatly improve the efficiency of charge separation, which is beneficial for rapid electrons transfer from Co_3O_4 NWs to ZIF9 for CO_2 $2e/2H^+$ reduction. This work opens the opportunity for CO_2 adsorption, activation and conversion with biomimetic PEC system to efficient resource utilization of CO_2 in the environmental field.

Acknowledgment

The authors appreciate the supports from the National Natural Science Foundation of China (NSFC, No. 21537003 and No. 21477085).

Appendix A. Supplementary data

Supplementary data associated with this article can be found, in the online version, at http://dx.doi.org/10.1016/j.apcatb.2016.08.008.

References

[1] A.M. Appel, J.E. Bercaw, A.B. Bocarsly, H. Dobbek, D.L. DuBois, M. Dupuis, J.G. Ferry, E. Fujita, R. Hille, P.J.A. Kenis, C.A. Kerfeld, R.H. Morris, C.H.F. Peden, A.R. Portis, S.W. Ragsdale, T.B. Rauchfuss, J.N.H. Reek, L.C. Seefeldt, R.K. Thauer, G.L. Waldrop, Chem. Rev. 113 (2013) 6621–6658.
[2] D. Xu, D. Wang, B. Li, X. Fan, X.W. Zhang, N.H. Ye, Y. Wang, S. Mou, Z. n. Zhuang, Environ. Sci. Technol. 49 (2015) 3548–3556.
[3] J.L. White, M.F. Baruch, J.E. Pander Iii, Y. Hu, I.C. Fortmeyer, J.E. Park, T. Zhang, K. Liao, J. Gu, Y. Yan, T.W. Shaw, E. Abelev, A.B. Bocarsly, Chem. Rev. 115 (2015) 12888–12935.
[4] H. Zhou, T. Fan, D. Zhang, ChemCatChem 3 (2011) 513–528.
[5] R.J. Lim, M.S. Xie, M.A. Sk, J.M. Lee, A. Fisher, X. Wang, K.H. Lim, Catal. Today 233 (2014) 169–180.
[6] W. Tu, Y. Zhou, Z. Zou, Adv. Mater. 26 (2014) 4607–4626.
[7] S. Xie, Q. Zhang, G. Liu, Y. Wang, Chem. Commun. 52 (2016) 35–59.
[8] D.-I. Won, J.-S. Lee, J.-M. Ji, W.-J. Jung, H.-J. Son, C. Pac, S.O. Kang, J. Am. Chem. Soc. 137 (2015) 13679–13690.
[9] J. Qiu, G. Zeng, M.A. Ha, M. Ge, Y. Lin, M. Hettick, B. Hou, A.N. Alexandrova, A. Javey, S.B. Cronin, Nano Lett. 15 (2015) 6177–6181.
[10] S. Wang, Z. Ding, X. Wang, Chem. Commun. 51 (2015) 1517–1519.
[11] Q. Kang, T. Wang, P. Li, L. Liu, K. Chang, M. Li, J. Ye, Angew. Chem. Int. Ed. 54 (2015) 841–845.
[12] D. Chen, X. Zhang, A.F. Lee, J. Mater. Chem. A 3 (2015) 14487–14516.
[13] M. Gattrell, N. Gupta, A. Co, J. Electroanal. Chem. 594 (2006) 1–19.
[14] M. Rakowski Dubois, D.L. Dubois, Acc. Chem. Res. 42 (2009) 1974–1982.
[15] Y. Liu, Y. Yang, Q. Sun, Z. Wang, B. Huang, Y. Dai, X. Qin, X. Zhang, ACS Appl. Mater. Interface 5 (2013) 7654–7658.
[16] K.S. Park, Z. Ni, A.P. Cote, J.Y. Choi, R. Huang, F.J. Uribe-Romo, H.K. Chae, M. O'Keeffe, O.M. Yaghi, Proc. Natl. Acad. Sci. U. S. A. 103 (2006) 10186–10191.
[17] Z. Zhang, Z.Z. Yao, S. Xiang, B. Chen, Energy Environ. Sci. 7 (2014) 2868–2899.
[18] S.B. Wang, X.C. Wang, Small 11 (2015) 3097–3112.
[19] R. Hinogami, S. Yotsuhashi, M. Deguchi, Y. Zenitani, H. Hashiba, Y. Yamada, Ecs Electrochem. Lett. 1 (2012) H17–H19.
[20] Y. Fu, D. Sun, Y. Chen, R. Huang, Z. Ding, X. Fu, Z. Li, Angew. Chem. Int. Ed. 51 (2012) 3364–3371.
[21] D.R. Sun, Y.H. Fu, W.J. Liu, L. Ye, D.K. Wang, L. Yang, X.Z. Fu, Z.H. Li, Chem. Eur. J. 19 (2013) 14279–14285.
[22] S. Wang, W. Yao, J. Lin, Z. Ding, X. Wang, Angew. Chem. Int. Ed. 53 (2014) 1034–1038.
[23] S.B. Wang, X.C. Wang, Angew. Chem. Int. Ed. 55 (2016) 2308–2320.
[24] Q. Liu, Z.X. Low, L. Li, A. Razmjou, K. Wang, J. Yao, H. Wang, J. Mater. Chem. A 1 (2013) 11563–11569.
[25] R. Li, J. Hu, M. Deng, H. Wang, X. Wang, Y. Hu, H.L. Jiang, J. Jiang, Q. Zhang, Y. Xie, Y. Xiong, Adv. Mater. 26 (2014) 4783–4788.
[26] S. Wang, J. Lin, X. Wang, Phys. Chem. Chem. Phys. 16 (2014) 14656–14660.
[27] X.F. Huang, T.C. Cao, M.C. Liu, G.H. Zhao, J. Phys. Chem. C 117 (2013) 26432–26440.
[28] Q. Shen, Z.F. Chen, X.F. Huang, M.C. Liu, G.H. Zhao, Environ. Sci. Technol. 49 (2015) 5828–5835.
[29] S. Gao, X. Jiao, Z. Sun, W. Zhang, Y. Sun, C. Wang, Q. Hu, X. Zu, F. Yang, S. Yang, L. Liang, J. Wu, Y. Xie, Angew. Chem. Int. Ed. 128 (2015) 708–712.
[30] S. Gao, Y. Lin, X. Jiao, Y. Sun, Q. Luo, W. Zhang, D. Li, J. Yang, Y. Xie, Nature 529 (2016) 68–71.
[31] R. Kuriki, K. Sekizawa, O. Ishitani, K. Maeda, Angew. Chem. Int. Ed. 54 (2015) 2406–2415.
[32] T. Arai, S. Sato, K. Uemura, T. Morikawa, T. Kajino, T. Motohiro, Chem. Commun. 46 (2010) 6944–6946.
[33] K. Sekizawa, K. Maeda, K. Domen, K. Koike, O. Ishitani, J. Am. Chem. Soc. 135 (2013) 4596–4605.
[34] T. Arai, S. Tajima, S. Sato, K. Uemura, T. Morikawa, T. Kajino, Chem. Commun. 47 (2011) 12664–12666.
[35] J.H. Jeon, P.M. Mareeswaran, C.H. Choi, S.I. Woo, RSC Adv. 4 (2014) 3016–3019.
[36] S. Sato, T. Arai, T. Morikawa, K. Uemura, T.M. Suzuki, H. Tanaka, T. Kajino, J. Am. Chem. Soc. 133 (2011) 15240–15243.
[37] R. Kuriki, H. Matsunaga, T. Nakashima, K. Wada, A. Yamakata, O. Ishitani, K. Maeda, J. Am. Chem. Soc. 138 (2016) 5159–5170.
[38] J. Gu, A. Wuttig, J.W. Krizan, Y. Hu, Z.M. Detweiler, R.J. Cava, A.B. Bocarsly, J. Phys. Chem. C 117 (2013) 12415–12422.
[39] W.W. Zhan, Q. Kuang, J.Z. Zhou, X.J. Kong, Z.X. Xie, L.S. Zheng, J. Am. Chem. Soc. 135 (2013) 1926–1933.
[40] S. Zhang, P. Kang, T.J. Meyer, J. Am. Chem. Soc. 136 (2014) 1734–1737.
[41] J.G. Velasco, Electroanalysis 9 (1997) 880–882.
[42] N. Kornienko, Y. Zhao, C.S. Kley, C. Zhu, D. Kim, S. Lin, C.J. Chang, O.M. Yaghi, P.D. Yang, J. Am. Chem. Soc. 137 (2015) 14129–14135.